Illumination compensation for image-domain wavefield tomography

Tongning Yang*, Jeffrey Shragge+, Paul Sava*
* *Center for Wave Phenomena, Colorado School of Mines*
+ *School of Earth and Environment, University of Western Australia*

ABSTRACT

Wavefield tomography represents a family of velocity model building techniques based on full waveforms as the input and seismic wavefields as the information carrier. When these techniques are implemented in the image domain and use seismic images as the input, they are referred to as image-domain wavefield tomography. The objective function for image-domain approach is designed to optimize the coherency of reflections in extended common-image gathers. The function applies a penalty operator to the gathers, thus highlighting image inaccuracies due to the velocity model error. Minimizing the objective function optimizes the model and improves the image quality, by making use of the gradient of the objective function computed using the adjoint-state method. Uneven illumination is a common problem for complex geological regions, such as sub-salt, or the consequence of incomplete data. Imbalanced illumination not only creates shadow zone for migrated images, but also results in defocusing in common-image gathers even when the migration velocity model is correct. This additional defocusing violates the wavefield tomography assumption stating that the migrated images are perfectly focused in the case of the correct model. Therefore, defocusing rising from illumination mixes with defocusing rising from the model errors and degrades the model reconstruction. We address this problem by incorporating the illumination effects into the penalty operator such that only the defocusing by model errors is used for model construction. This method improves the robustness and effectiveness of wavefield tomography applied in the areas characterized by poor illumination. Our synthetic examples demonstrate that velocity models are more accurately reconstructed by our method using the illumination compensation, leading to more coherent and better focused subsurface images than those in the conventional approach without illumination compensation.

Key words: wavefield tomography, illumination compensation, extended images, adjoint state method

1 INTRODUCTION

Building an accurate and reliable velocity model remains one of the biggest challenges in current seismic imaging practice. In regions characterized by complex subsurface structure, prestack wave-equation depth migration, (e.g., one-way wave-equation migration or reverse-time migration), is a powerful tool for accurately imaging the earth's interior (Gray et al., 2001; Etgen et al., 2009). The widespread use of these advanced imaging techniques drives the need for high-quality velocity models because these migration methods are very sensitive to model errors (Symes, 2008; Woodward et al., 2008; Virieux and Operto, 2009).

Wavefield tomography represents a family of techniques for velocity model building using seismic wavefields (Tarantola, 1984; Woodward, 1992; Pratt, 1999; Sirgue and Pratt, 2004; Plessix, 2006; Vigh and Starr, 2008; Plessix, 2009; Symes, 2009). The core of wavefield tomography is using a wave equation (typically constant density acoustic) to simulate wavefields as the information carrier. Wavefield tomog-

raphy is usually implemented in the data domain by adjusting the velocity model such that simulated and recorded data match (Tarantola, 1984; Pratt, 1999). This match is based on the strong assumption that the wave equation used for simulation is consistent with the physics of the earth. However, this is unlikely to be the case when the earth is characterized by strong (poro)elasticity. Significant effort is often directed toward removing the components of the recorded data that are inconsistent with the assumptions used.

Wavefield tomography can also be implemented in the image domain rather than in the data domain. Instead of minimizing the data misfit, the techniques in this category update the velocity model by optimizing the image quality, which is the cross-correlation of wavefields extrapolated from the source and receiver. The image quality is optimized when the data are migrated with the correct velocity model, as stated by the semblance principle (Al-Yahya, 1989; Yilmaz, 2001). The common idea is to optimize the coherency of reflection events in common-image gathers (CIGs) via velocity model updating. Since images are obtained using full seismograms, and velocity estimation also employs seismic wavefields as the information carrier, these techniques can be regarded as a particular type of wavefield tomography, and we refer to them as image-domain wavefield tomography. Unlike traditional ray-based reflection tomography methods, image-domain wavefield tomography uses band-limited wavefields in the optimization procedure. Thus, this technique is capable of handling complicated wave propagation phenomena such as multi-pathing in the subsurface. In addition, the band-limited character of the wave-equation engine more accurately approximates wave propagation in the subsurface and produces more reliable velocity updates.

Differential semblance optimization (DSO) is one realization of image-domain wavefield tomography. The essence of the method is to minimize the difference of the same reflection between neighboring offsets or angles. Symes and Carazzone (1991) propose a criterion for measuring coherency from offset gathers and establish the theoretic foundation for DSO. The concept is then generalized to space-lag (subsurface-offset) and angle-domain gathers (Shen and Calandra, 2005; Shen and Symes, 2008). Space-lag gathers (Rickett and Sava, 2002; Shen and Calandra, 2005) and angle-domain gathers (Sava and Fomel, 2003; Biondi and Symes, 2004) are two popular choices among various types of gathers used for velocity analysis. These gathers are obtained by wave-equation migration and are free of artifacts usually found in conventional offset gathers obtained by Kirchhoff migration, and thus they are suitable for applications in complex earth models (Stolk and Symes, 2004).

DSO implemented using space-lag gathers constructs a penalty operator which annihilates the energy at zero lag and enhances the energy at nonzero lags (Shen et al., 2003). This construction assumes that migrated images are perfectly focused at zero lag when the model is correct. If the model is incorrect, reflections in the gathers are defocused and the reflection energy spreads to nonzero lags. As a result, any energy left after applying the penalty is attributed to the result of model errors. However, this assumption is violated in practice when the subsurface illumination is uneven. Uneven illumination introduces additional defocusing such that images are not perfectly focused even if the velocity is correct, and it usually results from incomplete surface recorded data or from complex subsurface structure. Incomplete data cause loss of signal at some reflection angles and thus degrade the image. Nemeth et al. (1999) show that least-squared migration method can compensate the poor image quality due to the data deficiency. This method, however, is costly because of it requires many iterations to converge (Shen et al., 2011). In complex subsurface regions, such as sub-salt, uneven illumination is a general problem and it deteriorates the quality of imaging and velocity model building (Leveille et al., 2011). Gherasim et al. (2010) and Shen et al. (2011) show that the quality of migrated images can be optimized by illumination-based weighting generated from a demigration/remigration procedure. Tang and Biondi (2011) compute the diagonal of the Hessian matrix for the migration operator and use it for illumination compensation of the image before velocity analysis. These approaches effectively improve the quality of subsurface images, especially the balance of the amplitude. Nonetheless, they do not investigate the negative impact of illumination on the velocity model building. Furthermore, the misleading velocity updates due to uneven illumination remains an unsolved problem.

In this paper we address the problem of uneven illumination associated with image-domain wavefield tomography. We first review the theory for wavefield tomography in the image-domain including the formulation of the objective function and the gradient calculation. Next we explain how the uneven illumination affects the focusing of space-lag gathers and breaks down the assumption for DSO. We then propose a solution to this problem by using the illumination information in the construction of the penalty operator which is an integral part of the objective function. We illustrate our method with two synthetic examples representing two different types of illumination problems.

2 THEORY

In image-domain wavefield tomography using space-lag extended images (subsurface-offset CIGs), we formulate an objective function and compute its gradient using the adjoint-state method (Plessix, 2006; Symes, 2009). We discuss this method in detail and then analyze the influence of the illumination on gather focusing and how it impacts wavefield tomography. We conclude this section by introducing our solution to the illumination problem for wavefield tomography.

For simplicity, we discuss the methodology in the frequency-domain rather than in the time-domain although the latter is completely equivalent and analogous. We formulate the inverse problem by first defining the state variables, through which the objective function is related to the model parameter. The state variables for our problem are the source and receiver wavefields u_s and u_r obtained by solving the fol-

lowing acoustic wave equation:

$$\begin{bmatrix} \mathcal{L}(\mathbf{x},\omega,m) & 0 \\ 0 & \mathcal{L}^*(\mathbf{x},\omega,m) \end{bmatrix} \begin{bmatrix} u_s(j,\mathbf{x},\omega) \\ u_r(j,\mathbf{x},\omega) \end{bmatrix} = \begin{bmatrix} f_s(j,\mathbf{x},\omega) \\ f_r(j,\mathbf{x},\omega) \end{bmatrix} , \tag{1}$$

where f_s is a point or plane source, f_r are the record data, $j = 1, 2, ..., N_s$ where N_s is the number of shots, ω is the angular frequency, and $\mathbf{x}$ are the space coordinates $\{x, y, z\}$. The wave operator $\mathcal{L}$ and its adjoint $\mathcal{L}^*$ propagate the wavefields forward and backward in time respectively using a two-way wave equation. Thus, $\mathcal{L}$ is formulated as

$$\mathcal{L} = -\omega^2 m - \Delta , \tag{2}$$

where Δ is the Laplace operator, and m represents the model (slowness squared).

In the second step of the adjoint-state method, we construct the objective function from which we derive the adjoint sources used to model the adjoint-state variables required by the gradient computation. The objective function for image-domain wavefield tomography is defined using the semblance principle (Yilmaz, 2001) and measures the image incoherency caused by the model errors. Therefore, the inversion simultaneously reconstructs the model and improves the image quality by minimizing the objective function.

The objective function based on space-lag CIGs is

$$\mathcal{H}_{\boldsymbol{\lambda}} = \frac{1}{2} \| K_I(\mathbf{x}) P(\boldsymbol{\lambda}) r(\mathbf{x},\boldsymbol{\lambda}) \|^2_{\mathbf{x},\boldsymbol{\lambda}} , \tag{3}$$

and

$$\begin{aligned} r(\mathbf{x},\boldsymbol{\lambda}) &= \sum_j \sum_\omega \overline{u_s(j,\mathbf{x}-\boldsymbol{\lambda},\omega)} u_r(j,\mathbf{x}+\boldsymbol{\lambda},\omega) \\ &= \sum_j \sum_\omega T(-\boldsymbol{\lambda}) \overline{u_s(j,\mathbf{x},\omega)} T(\boldsymbol{\lambda}) u_r(j,\mathbf{x},\omega) , \end{aligned} \tag{4}$$

where the overline represents complex conjugate. The operator T represents the space shift applied to the wavefields and is defined by

$$T(\boldsymbol{\lambda}) u(j,\mathbf{x},\omega) = u(j,\mathbf{x}+\boldsymbol{\lambda},\omega) , \tag{5}$$

The mask operator $K_I(\mathbf{x})$ limits the construction of the gathers to select locations in the subsurface. The penalty operator $P(\boldsymbol{\lambda})$ annihilates the focused energy at zero lag and highlights the energy of residual moveout at nonzero lag (Shen and Symes, 2008):

$$P(\boldsymbol{\lambda}) = |\boldsymbol{\lambda}| . \tag{6}$$

In practice, it is common to restrict the space-lags in the horizontal directions only, i.e. $\boldsymbol{\lambda} = \{\lambda_x, \lambda_y, 0\}$. The objective function $\mathcal{H}_{\boldsymbol{\lambda}}$ is minimized when the reflections focus at zero lag, which is an indication of the correct velocity model.

The adjoint sources are computed as the derivatives of the objective function $\mathcal{H}_{\boldsymbol{\lambda}}$ shown in equation 3 with respect to the state variables u_s and u_r:

$$\begin{bmatrix} g_s(j,\mathbf{x},\omega) \\ g_r(j,\mathbf{x},\omega) \end{bmatrix} = \begin{bmatrix} \sum\limits_{\boldsymbol{\lambda}} T(\boldsymbol{\lambda}) P(\boldsymbol{\lambda}) \; K_I(\mathbf{x}) \overline{K_I(\mathbf{x}) P(\boldsymbol{\lambda}) r(\mathbf{x},\boldsymbol{\lambda})} T(\boldsymbol{\lambda}) u_r(j,\mathbf{x},\omega) \\ \sum\limits_{\boldsymbol{\lambda}} T(-\boldsymbol{\lambda}) P(\boldsymbol{\lambda}) \; K_I(\mathbf{x}) \overline{K_I(\mathbf{x}) P(\boldsymbol{\lambda})} r(\mathbf{x},\boldsymbol{\lambda}) T(-\boldsymbol{\lambda}) u_s(j,\mathbf{x},\omega) \end{bmatrix} . \tag{7}$$

The adjoint state variables a_s and a_r are the wavefields obtained by backward and forward modeling, respectively, using the corresponding adjoint sources defined in equation 7:

$$\begin{bmatrix} \mathcal{L}^*(\mathbf{x},\omega,m) & 0 \\ 0 & \mathcal{L}(\mathbf{x},\omega,m) \end{bmatrix} \begin{bmatrix} a_s(j,\mathbf{x},\omega) \\ a_r(j,\mathbf{x},\omega) \end{bmatrix} = \begin{bmatrix} g_s(j,\mathbf{x},\omega) \\ g_r(j,\mathbf{x},\omega) \end{bmatrix} , \tag{8}$$

where $\mathcal{L}$ and $\mathcal{L}^*$ are the same wave propagation operators used in equation 1.

The last step of the gradient computation is simply the correlation between state variables and adjoint state variables:

$$\frac{\partial \mathcal{H}_{\boldsymbol{\lambda}}}{\partial m} = \sum_j \sum_\omega \frac{\partial \mathcal{L}}{\partial m} \left(u_s(j,\mathbf{x},\omega) \overline{a_s(j,\mathbf{x},\omega)} + u_r(j,\mathbf{x},\omega) \overline{a_r(j,\mathbf{x},\omega)} \right) , \tag{9}$$

where $\frac{\partial \mathcal{L}}{\partial m}$ is the partial derivative of the wave propagation operator with respect to the model parameter. Using the definition of $\mathcal{L}$ in equation 2, we find that $\frac{\partial \mathcal{L}}{\partial m} = -\omega^2$. From equation 9 one may notice that the gradient for image-domain wavefield tomography consists of two correlations because we define both the source and receiver wavefields as the state variables.

The derivation above shows the construction of the image-domain wavefield tomography objective function and its gradient. Given these two components, the solution to the inverse problem is found by minimizing the objective function using non-linear gradient-based iterative methods (Knyazev and Lashuk, 2007). In each iteration, the gradient is computed and the model update is calculated by a line search in the steepest descent or conjugate gradient directions.

To analyze the illumination effects on focusing, we first illustrate the focusing mechanism for reflections in space-lag gathers. Yang and Sava (2010) derive the analytic formula for the reflection moveout in the extended images. Assuming constant local velocity, a reflection in space-lag gathers obtained by migrating one shot experiment is a straight line in 2D and a plane in 3D:

$$z(\boldsymbol{\lambda}) = d_0 - \frac{\tan\theta \, (\mathbf{q} \cdot \boldsymbol{\lambda})}{n_z} . \tag{10}$$

Here d_0 represents the depth of the reflection corresponding to the chosen CIGs location, $\boldsymbol{\lambda}$ represents the horizontal space lag $\boldsymbol{\lambda} = \{\lambda_x, \lambda_y, 0\}$, n_z is the vertical component of the unit vector normal to the reflection plane, $\mathbf{q}$ is the unit vector parallel to the reflection plane, and θ is the reflection angle. When we stack the gathers obtained with a correct model from all available shots, the straight lines or planes corresponding to reflections from different shots are superimposed and interfere to form a focused point at zero lag (Yang and Sava, 2010). Good

interference of such events, however, occurs only if the reflector point is well illuminated by the experiments from the surface. In other words, the surface shot coverage must be large enough and regularly distributed. Also, the subsurface illumination must be even so that the reflector is illuminated on a sufficient range of reflection angles from the surface. If either of these conditions is not satisfied, the reflection energy does not interfere perfectly and the gathers defocus, even if the correct model is used for the imaging.

We conclude that the defocusing of reflections in the space-lag gathers may result from velocity errors, as well as from the imperfect stacking due to uneven illumination. In general, these two different kinds of defocusing are indistinguishable to the velocity analysis procedure. The penalty operator in equation 6 emphasizes all energy away from zero lag and includes both the defocusing caused by the velocity error and by the uneven illumination. Thus, the penalty operator leads to a residual that is much larger than what would be expected for a given error in the model. Penalizing the defocusing due to the illumination misleads the inversion and results in overcorrection and artificial updates.

To alleviate the negative influence of uneven illumination, we need to include the illumination information in the tomographic procedure. One approach uses the illumination information as a weighting function to preconditioning the gathers. The gathers in poor illumination areas are down-weighted as the defocusing information is less reliable than the gathers in good illumination areas. This approach stabilizes the inversion but decreases the accuracy of the results as the useful velocity information in poor illumination areas is ignored. The poor illumination area, however, is exactly the place where we want to make use of all available information for the model building. To overcome the illumination problem and preserve the useful information in the tomography, we introduce a new illumination-based penalty operator to replace the conventional DSO penalty operator. The new operator is constructed such that it only emphasizes the defocusing caused by the velocity error and ignores the defocusing caused by uneven illumination. To achieve this goal, we analyze the image defocusing due to uneven illumination by applying illumination analysis.

Illumination analysis in the framework of wave-equation migration is formulated using the solution to migration deconvolution problems (Yu and Schuster, 2003). Migration deconvolution first establishes a linear relationship between a reflectivity distribution $\tilde{r}$ and seismic data d:

$$\mathcal{M}\tilde{r}\left(\mathbf{x}\right) = d \ , \tag{11}$$

where $\mathcal{M}$ represents a forward Born modeling operator which is linear with respect to the reflectivity. A migrated image is obtained by applying the adjoint of the modeling operator $\mathcal{M}^*$ to the data,

$$\mathcal{M}^* d = \mathcal{M}^*\mathcal{M}\tilde{r}\left(\mathbf{x}\right) = r\left(\mathbf{x}\right) \ , \tag{12}$$

where r is a migrated image. Note that the migrated image is the result of blurring the reflectivity $\tilde{r}$ by $(\mathcal{M}^*\mathcal{M})$, which is the Hessian (second-order derivative of the operator with respect to the model) for the operator $\mathcal{M}$. Thus, the reflectivity can be computed from the migrated image by

$$\tilde{r}\left(\mathbf{x}\right) = \left(\mathcal{M}^*\mathcal{M}\right)^{-1} r\left(\mathbf{x}\right) \ , \tag{13}$$

where $\left(\mathcal{M}^*\mathcal{M}\right)^{-1}$ includes the subsurface illumination information associated with the velocity structure and acquisition geometry. In practice, the full $\left(\mathcal{M}^*\mathcal{M}\right)^{-1}$ matrix is too costly to construct, but we can evaluate its impact by applying a cascade of demigration and migration $(\mathcal{M}^*\mathcal{M})$ to a reference image:

$$r_e\left(\mathbf{x}\right) = \mathcal{M}^*\mathcal{M}r\left(\mathbf{x}\right) \ . \tag{14}$$

The resulting image r_e approximates the diagonal elements of the Hessian as the illumination effects, and can be used as a weight for illumination compensation of migrated image (Guitton, 2004; Gherasim et al., 2010; Tang and Biondi, 2011). equation 14 only computes the illumination effects distributed at image points. In our problem, we are concerned with the defocusing caused by the illumination in the space-lag gathers, and need to evaluate the illumination effects at image points and along their space-lag extension. Using the concept of extended modeling (Symes, 2008), we can generalize equation 12 to the extended space $\mathbf{x} - \boldsymbol{\lambda}$:

$$r_e\left(\mathbf{x}, \boldsymbol{\lambda}\right) = \mathcal{M}^*\mathcal{M}r\left(\mathbf{x}, \boldsymbol{\lambda}\right) \ , \tag{15}$$

where $r_e\left(\mathbf{x}, \boldsymbol{\lambda}\right)$ are space-lag gathers containing reference image at zero space lag, and r_e are the output gathers containing defocusing associated with illumination effects. Such defocusing is the consequence of uneven illumination and should not be penalized by the penalty operator in the velocity updating process. Therefore, an illumination-based penalty operator can be constructed as

$$P\left(\mathbf{x}, \boldsymbol{\lambda}\right) = \frac{1}{E[r_e\left(\mathbf{x}, \boldsymbol{\lambda}\right)] + \epsilon} \ , \tag{16}$$

where E represents envelope and ϵ is a damping factor used to stabilize the division. By definition, this penalty operator has low values in the area of defocusing due to uneven illumination and high values in the rest. Thus, this operator is consistent with our idea of avoiding penalty to reflection energy irrelevant to velocity errors, e.g., the artifacts caused by illumination. Replacing the conventional penalty in equation 6 with the one in equation 16 is the basis for our illumination compensated image-domain wavefield tomography. Note that the DSO penalty operator is a special case of our new penalty operator and corresponds to the case of perfect subsurface illumination and wide-band data.

3 EXAMPLES

In this section, we use two synthetic examples to illustrate our illumination compensated image-domain wavefield tomography. In the first example, we use incomplete data to simulate illumination problems due to the acquisition. In the second example, we use the Sigsbee model to test our method in regions of complex geology with poor subsurface illumination caused by irregular salt.

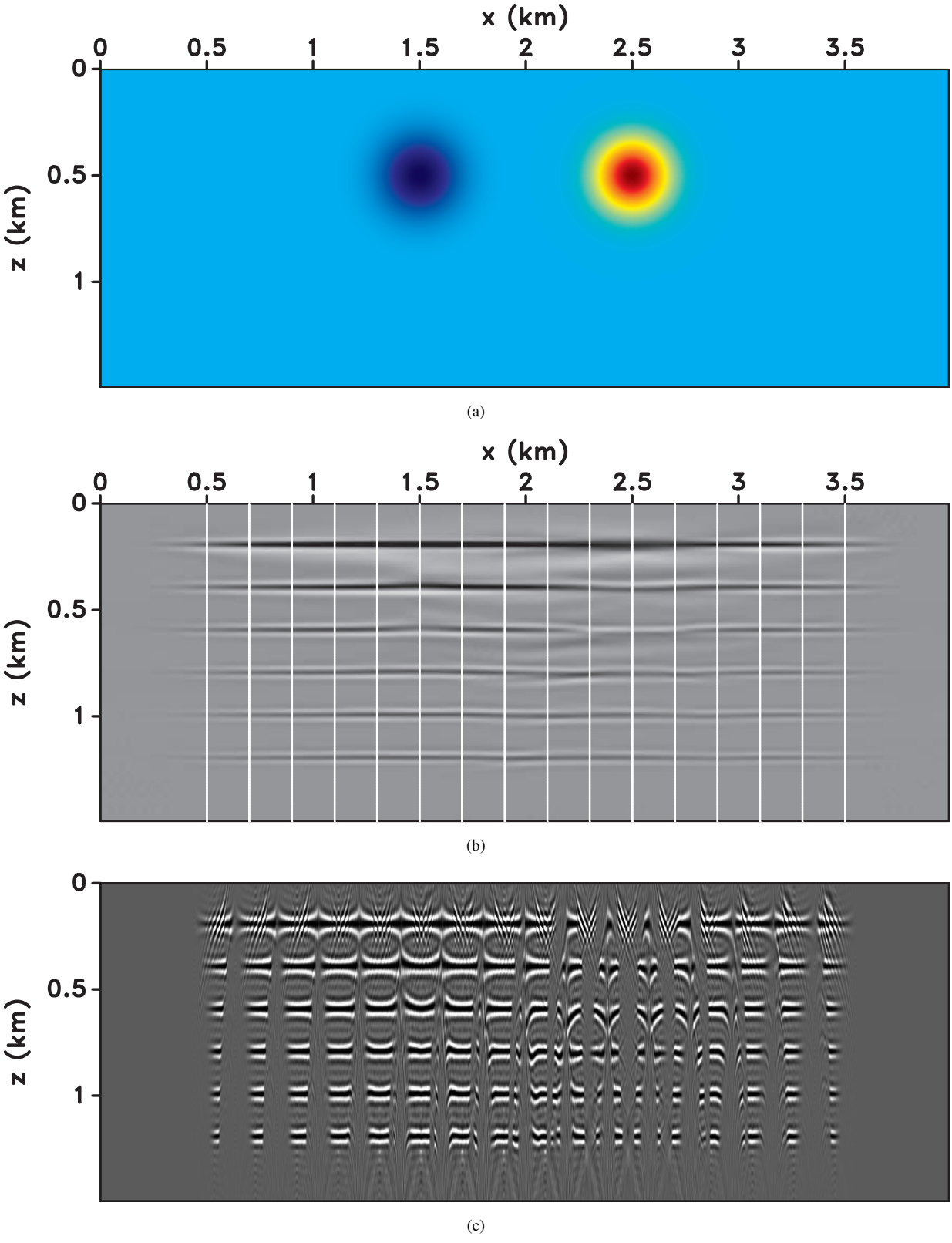


Figure 1. (a) The true model used to generate the data, (b) the migrated image, and (c) the angle-domain gathers obtained using the true model.

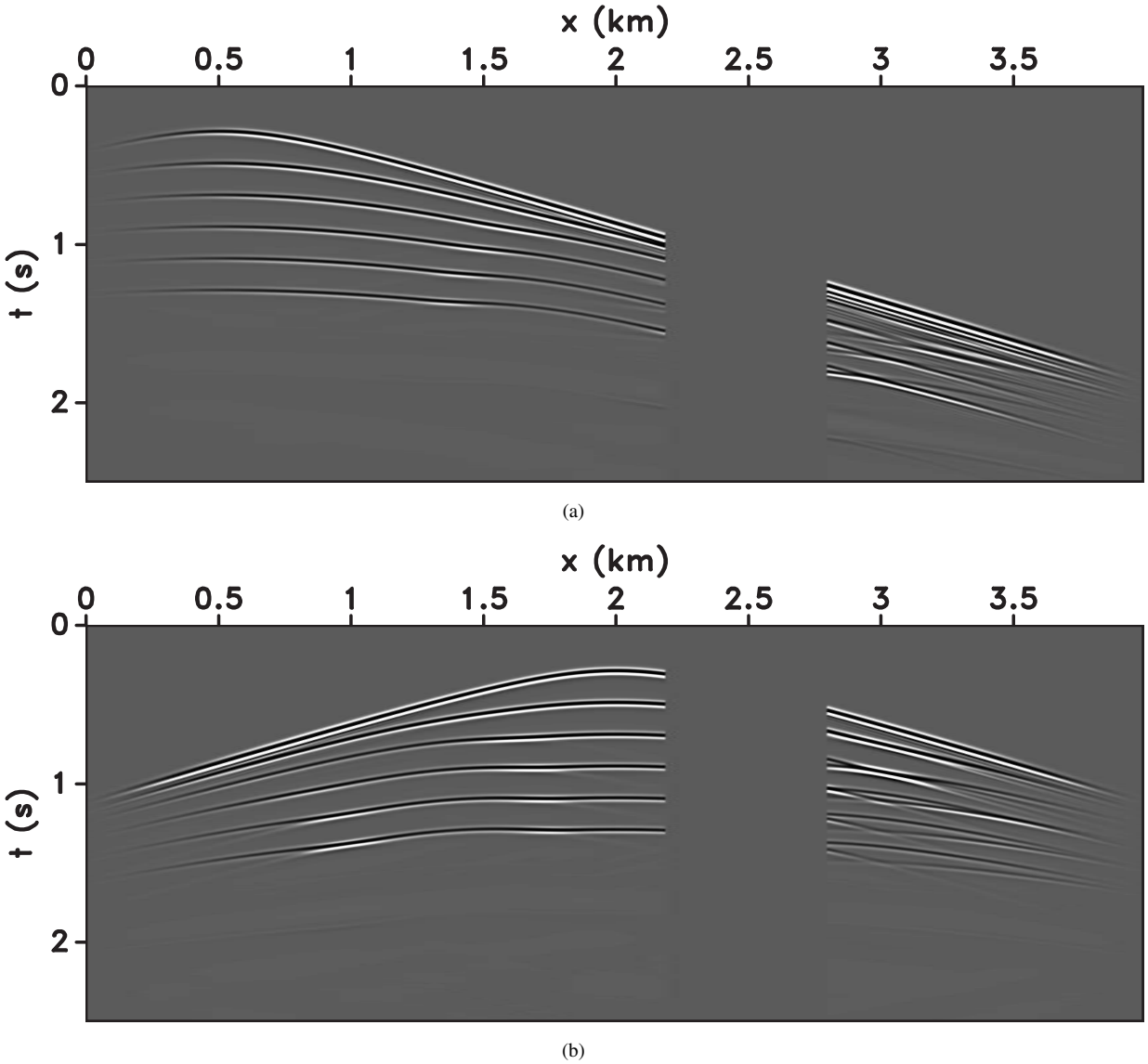


Figure 2. Two shot gathers at (a) 0.5 km and (b) 2.0 km showing a gap of 0.6 km in the acquisition surface. The gap simulate an obstacle which prevents data acquisition, e.g., a drilling platform.

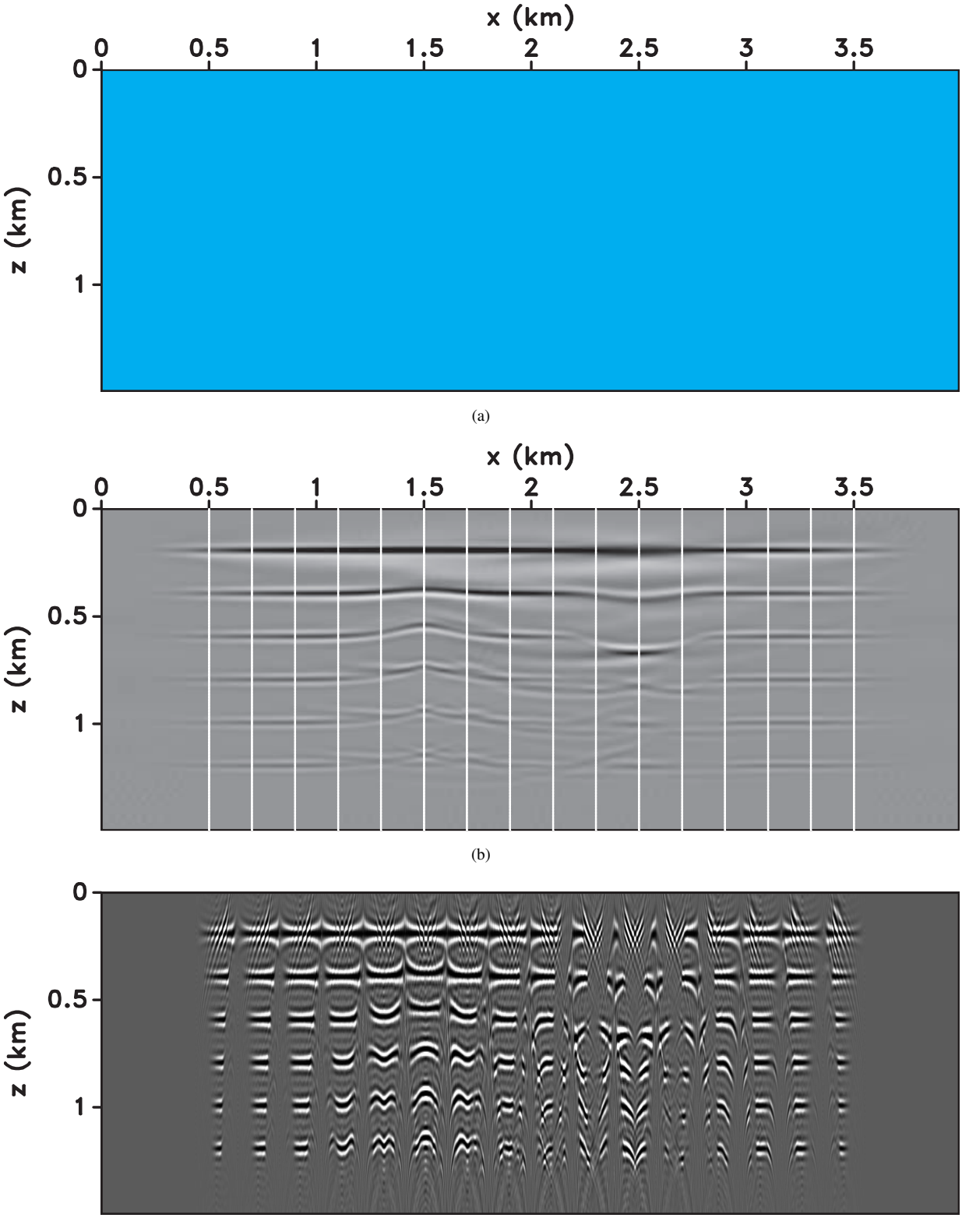
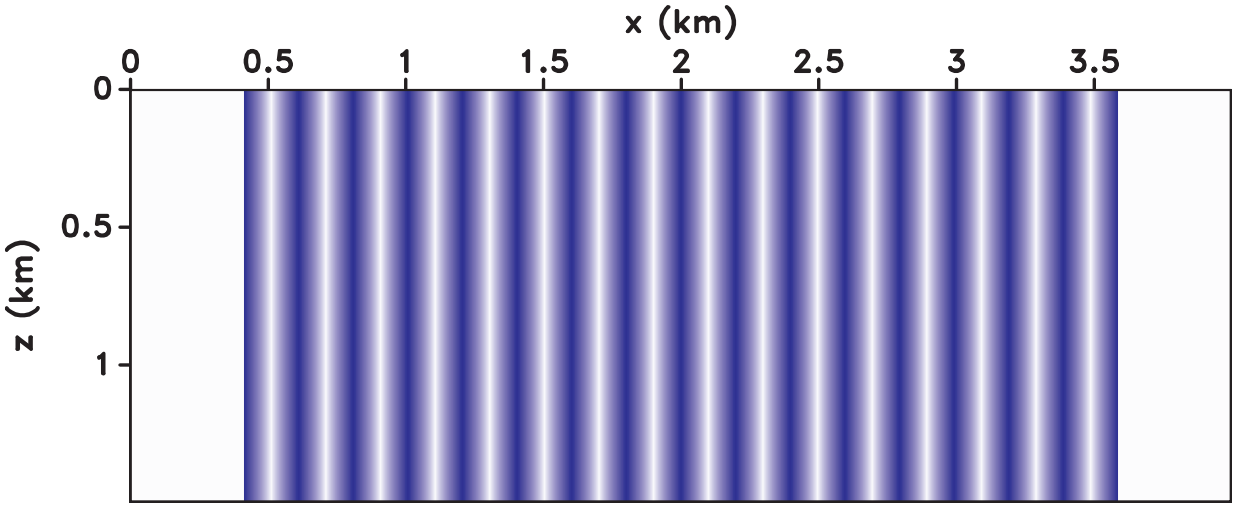
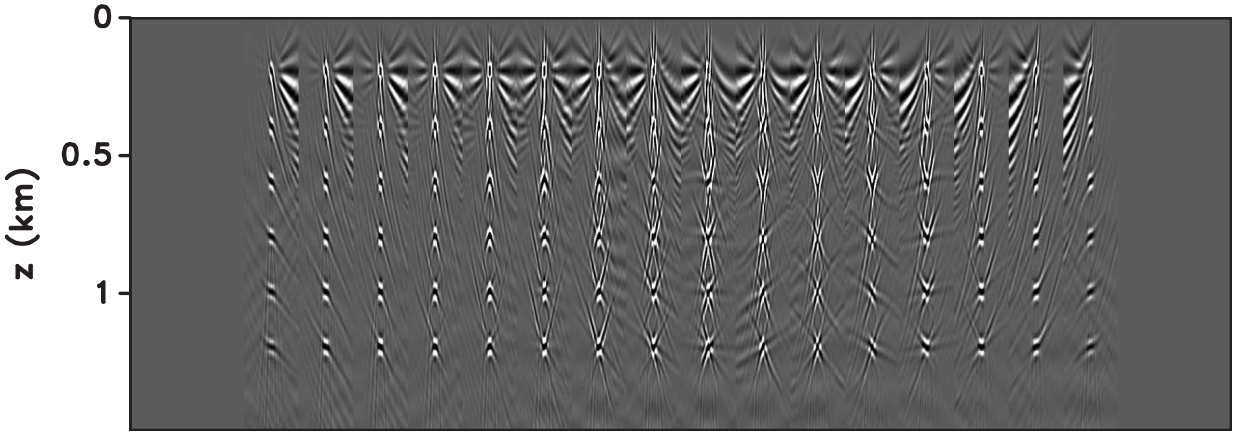


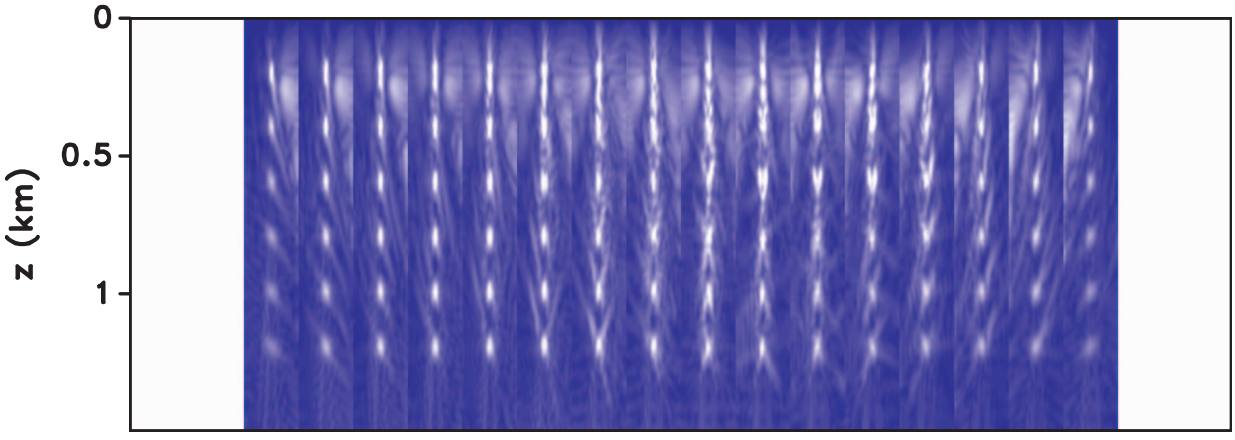
Figure 3. (a) The initial constant model, (b) the migrated image, and (c) the angle-domain gathers obtained using the initial model.



(a)

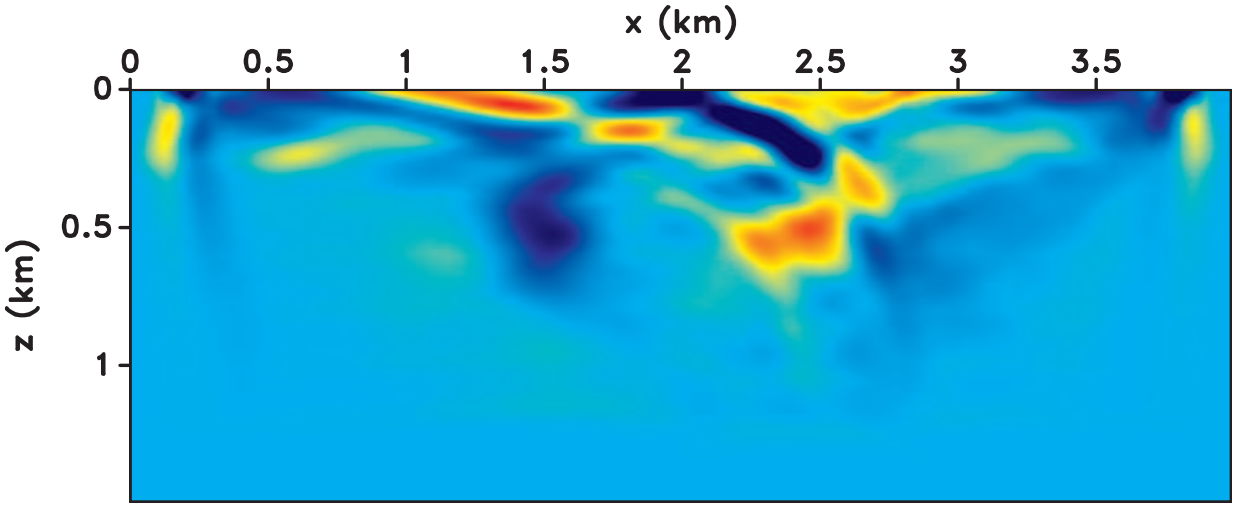


(b)

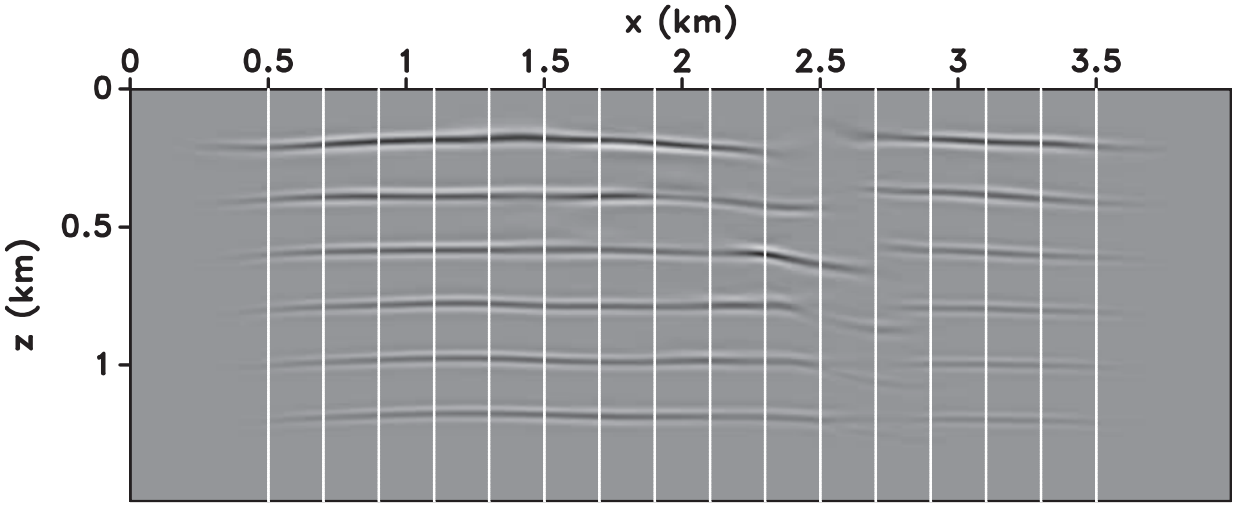


(c)

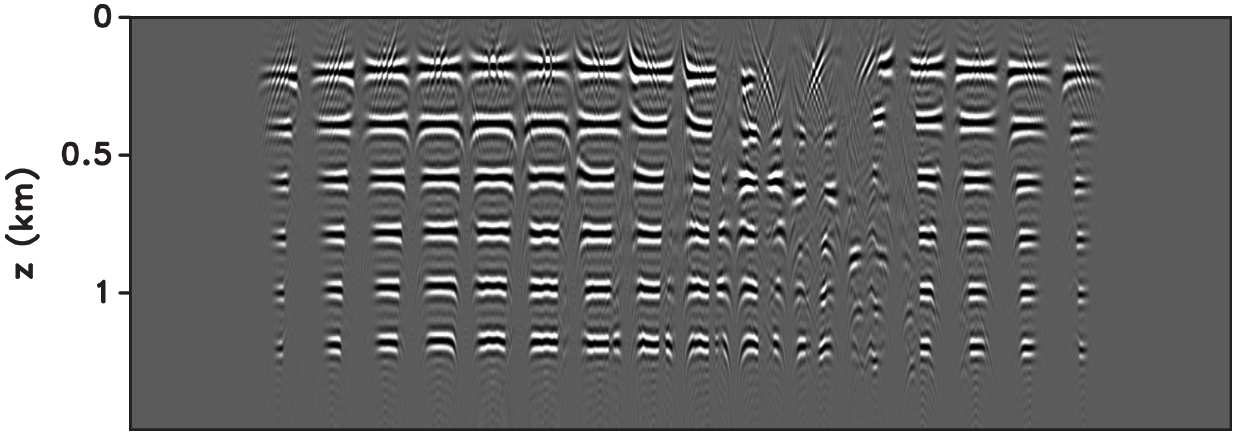
Figure 4. (a) The conventional DSO penalty operator. (c) The gathers obtained with demigration/migration showing the illumination effects. (d) The illumination-based penalty operator constructed from the gathers in Figure 4(c). The light areas cover the defocusing due to the illumination.



(a)

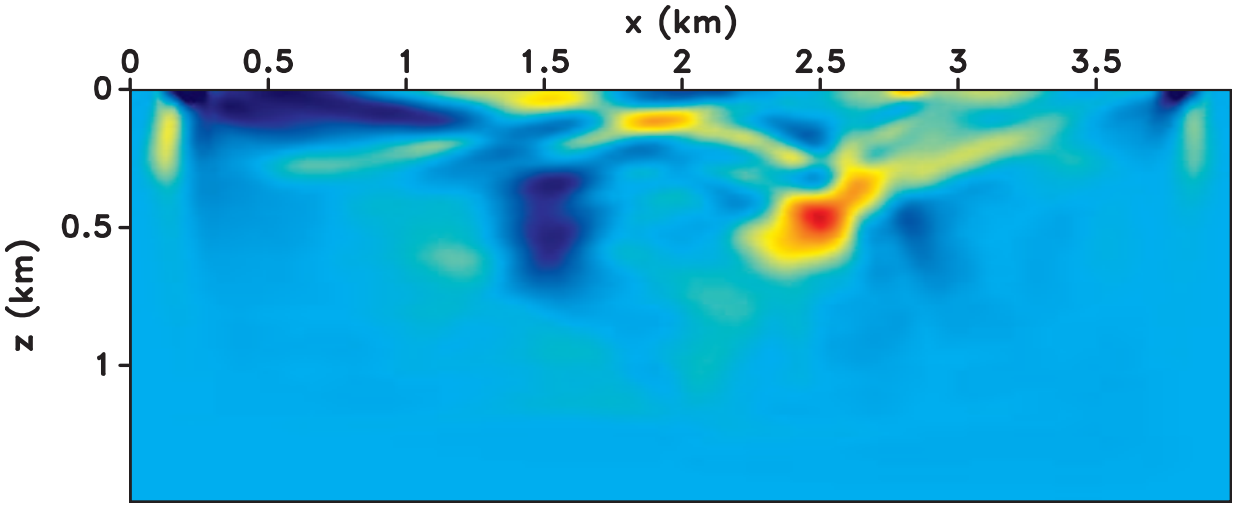


(b)

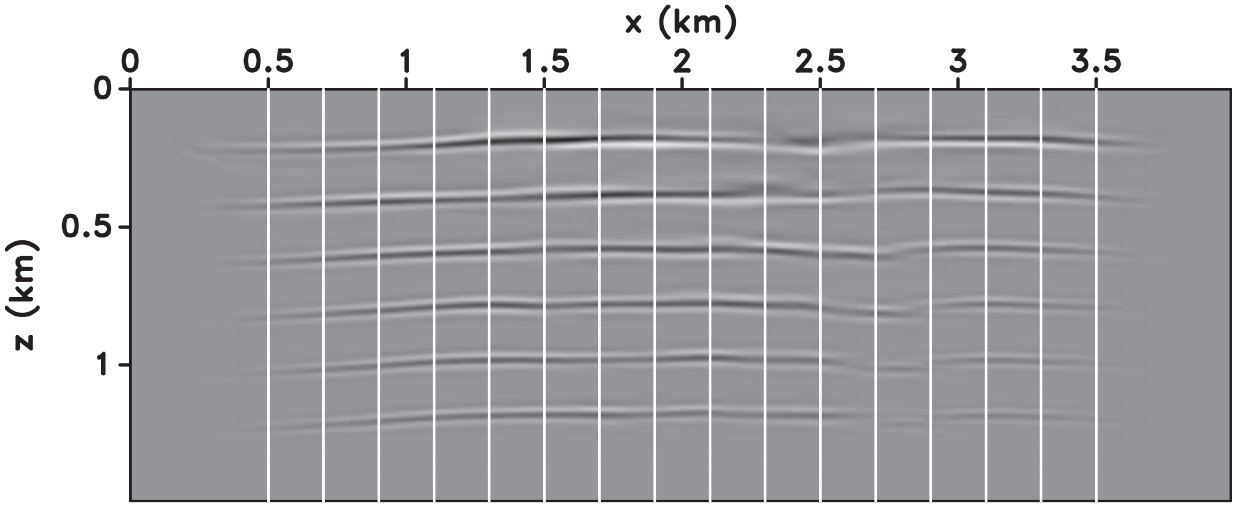


(c)

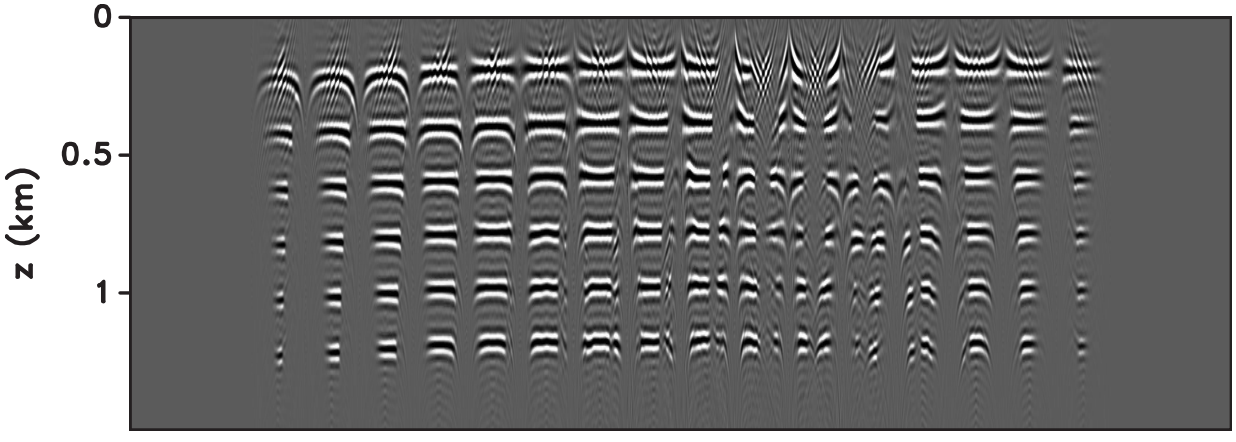
Figure 5. (a) The reconstructed model using conventional DSO penalty, (b) the migrated image, and (c) the angle-domain gathers obtained using the reconstructed model.



(a)



(b)



(c)

Figure 6. (a) The reconstructed model using the illumination-based penalty, (b) the migrated image, and (c) the angle-domain gathers obtained using the reconstructed model.

The velocity model for the first example is shown in Figure 1(a). For five horizontal interfaces simulated as density contrasts, we generate the data at receivers distributed along the surface. Two shot gathers are shown in Figures 2(a) and 2(b). The data are truncated from $2.2 - 2.8$ km to simulate an acquisition gap. The initial model is constant (Figures 3(a)). The migrated image and angle-domain gathers for the true and initial models are shown in Figures 1(b)-1(c) and Figures 3(b)-3(c), respectively. Note that the angle gathers are displayed at selected locations corresponding to the vertical bars overlain in Figures 1(b) and 3(b). The migrated image for the initial model shows defocusing and crossing events caused by the incorrect model. The illumination gap due to the missing data and the residual moveout caused by the wrong velocity can be observed on the angle gathers shown in Figure 3(c).

For comparison with our method, we run the inversion using conventional DSO penalty operator. Figure 9(a) plots the penalty operators at the same selected locations shown in Figure 1(b). The actual spacing of the gathers and penalty operators are 0.2 km. Since the conventional penalty is laterally invariant, the figure consists of the same operators duplicated at different lateral position. The inverted model after 30 nonlinear iterations is plotted in Figure 5(a), and the corresponding migrated image and angle gathers are shown in Figure 5(b) and 5(c). The reconstruction of the model is not satisfactory, especially for the anomaly under the acquisition gap. Also, the model contains many artifacts as the consequence of the incomplete data. As a result, the reduced quality of the image obtained with the inverted model is not surprising. Although the reflections on the left of the image are quite continuous and flat, those on the right, especially under the acquisition gap, are not flat and are even discontinuous. This result clearly shows the negative impact of the poor illumination on image-domain wavefield tomography.

To show the defocusing due to illumination effects in the gathers, we construct the space-lag gathers with the current image in Figure 3(b) at zero-lag as the reference image gathers. We apply the demigration/migration workflow from equation 15 to the reference gathers. The result, as shown in Figure 4(b), characterizes the illumination effects given the velocity model and acquisition setup. Most reflection energy is focused, thus indicating good illumination, but we can still observe defocusing as the consequence of incomplete data in the area under the acquisition gap. The illumination-based penalty operator is constructed from the gathers in Figure 4(b) using equation 16, as plotted in Figure 4(c). We can observe that the areas in light color coincide with the focused energy at zero lag and defocusing away from zero lag in Figure 4(b). Thus, the penalty operator does not emphasize the defocusing due to the uneven illumination and highlights only the defocusing due to velocity errors.

Using the new penalty operator, we update the model under the same conditions as in the example using DSO, Figure 6(a). Compared with the result in Figure 5(a), the result obtained with the new penalty is cleaner and contains fewer artifacts. Also, the anomaly under the acquisition gap is more accurately reconstructed and closer to the true model. Because of the improved model, the images are also improved, as seen in Figure 6(b). The reflections under the acquisition gap are more continuous and flat than the image in Figure 5(b). In addition, one can observe from the angle gathers in Figure 6(c) that more events appear in the area under the acquisition gap and overall reflections are flatter, which indicates an improved signal-to-noise ratio rising from the more accurate reconstructed model.

We also apply our method to the Sigsbee 2A model (Paffenholz et al., 2002), and concentrate on the subsalt region. The target area ranges from $x = 6.5 - 20$ km, and from $z = 4.5 - 9$ km. The model, migrated image, and angle-domain gathers for correct and initial models are shown in Figures 7(a)-7(c) and Figures 8(a)-8(c), respectively. The angle gathers are displayed at selected locations corresponding to the vertical bars overlain in Figures 7(b) and 8(b). The actual spacing of the gathers and penalty operators are 0.45 km. Note that the reflections in the angle gathers appear only at positive angles, as the data are simulated for towed streamers and the subsurface is illuminated from one side only. Just as for the previous example, we run the inversion using both the conventional DSO penalty and the illumination-based penalty operators. The DSO penalty operator is shown in Figure 9(a). For the illumination-based operator, we first generate gathers containing defocusing due to illumination (Figure 9(b)), and then we construct the penalty operator using equation 16 as shown in Figure 9(c). From the gathers characterizing the illumination effects, we can observe the significant defocusing in the subsalt area as the salt distorts the wavefields used for imaging and causes the poor illumination in this area.

We run both inversions for 10 iterations, and obtain the reconstructed model, migrated image, and angle-domain gathers shown in Figures 10(a)- 10(c) and Figures 11(a)-11(c), respectively. The figures show that we update the models in the correct direction in both cases and that the reconstructed models are closer to the true model than the starting model. We find, however, that the model obtained using the illumination-based penalty is closer to the true model than the model obtained using DSO penalty. The DSO model is not sufficiently updated and is too slow. This is because the severe defocusing due to the salt biases the inversion when we do not take into accounts the uneven illumination for tomography. The comparison of the images also suggests that the inversion using the illumination-based penalty is superior to the inversion using DSO penalty. Both the images are improved due to the updated model, as illustrated, for example, by that the diffractors distributed at $z = 7.6$ km focus, and the faults located between $x = 14.0$ km, $z = 6.0$ km and $x = 16.0$ km, $z = 9.0$ km are more visible in the images. If we concentrate on the bottom reflector (around 9 km), we can distinguish the extent of the improvements on the image quality for both inversions. The bottom reflector is corrected to the right depth for inversion using the illumination-based penalty, while the bottom reflector for inversion using DSO penalty is still away from the right depth and not as flat as the reflector in Figure 11(b). Figures 12(a)-12(d) compare the angle gathers at $x = 10.2$ km for the correct, initial, and reconstructed models using DSO

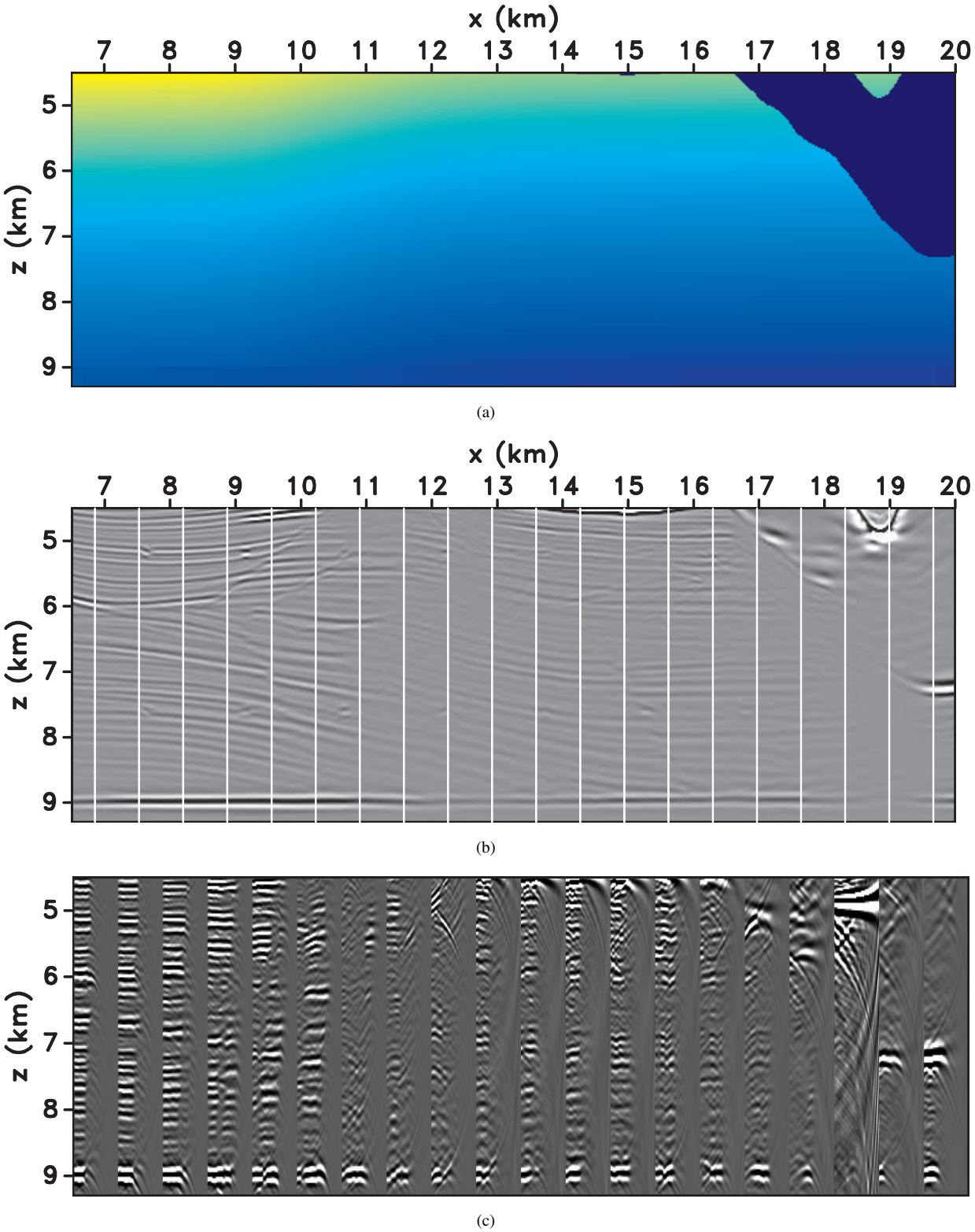


Figure 7. (a) The true model in the target area of the Sigsbee model. (b) The migrated image, and (c) the angle-domain gathers obtained using the true model.

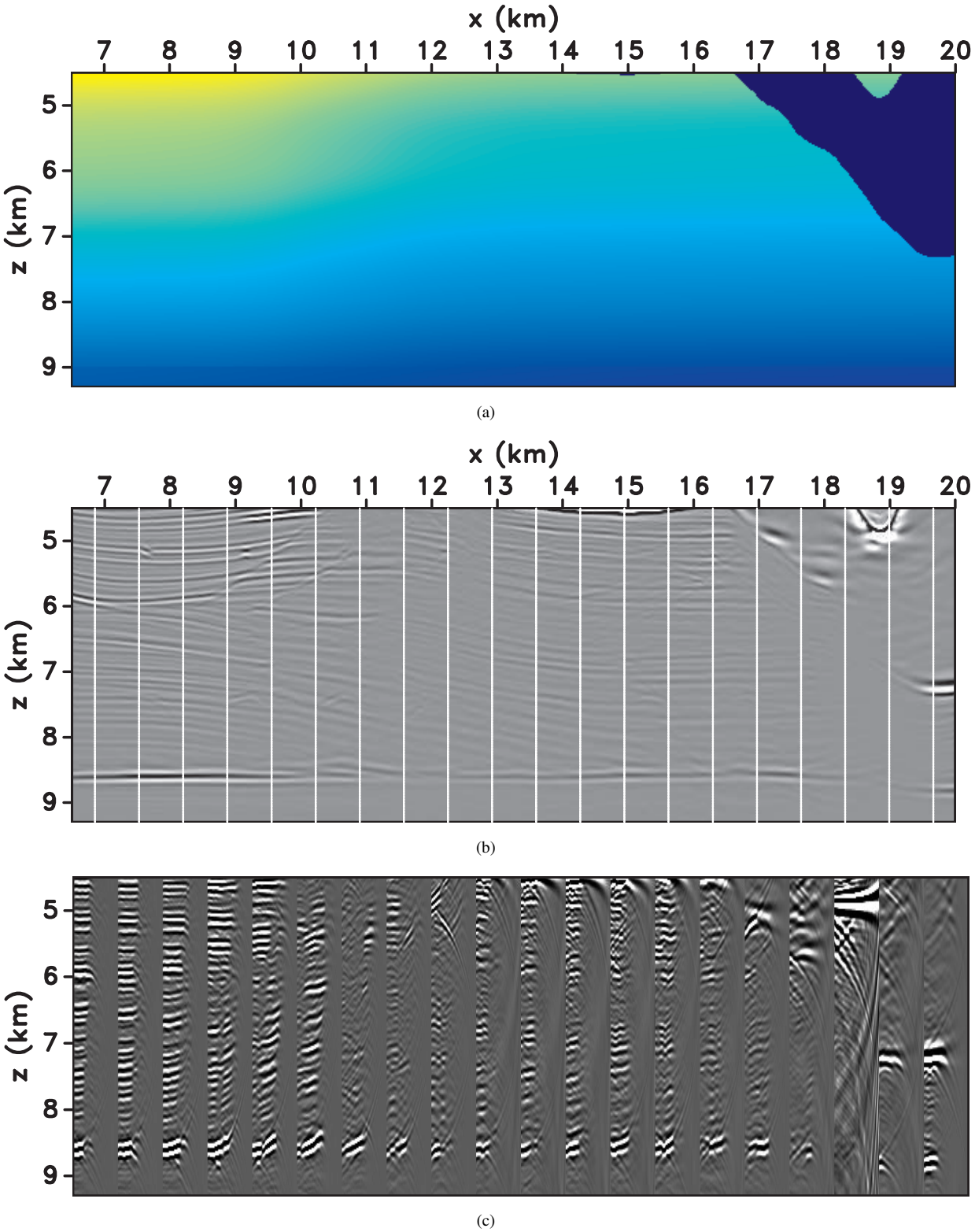


Figure 8. (a) The initial model obtained by scaling the true model. (b) The migrated image, and (c) the angle-domain gathers obtained using the initial model.

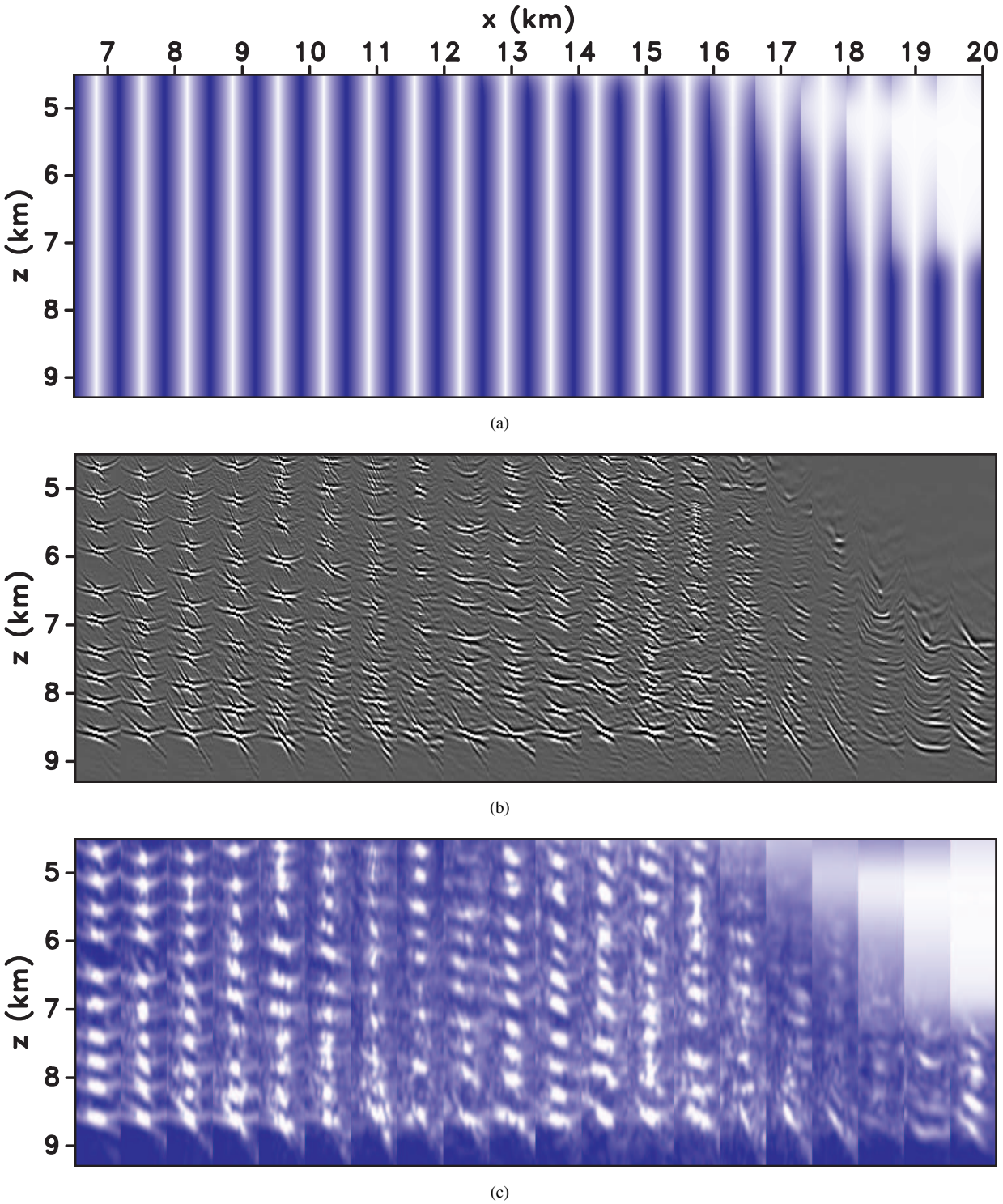


Figure 9. (a) The conventional DSO penalty operator. (b) The gathers obtained with demigration/migration showing the illumination effects. (c) The illumination-based penalty operator constructed from the gathers in Figure 9(b). The light areas cover the defocusing due to the illumination.

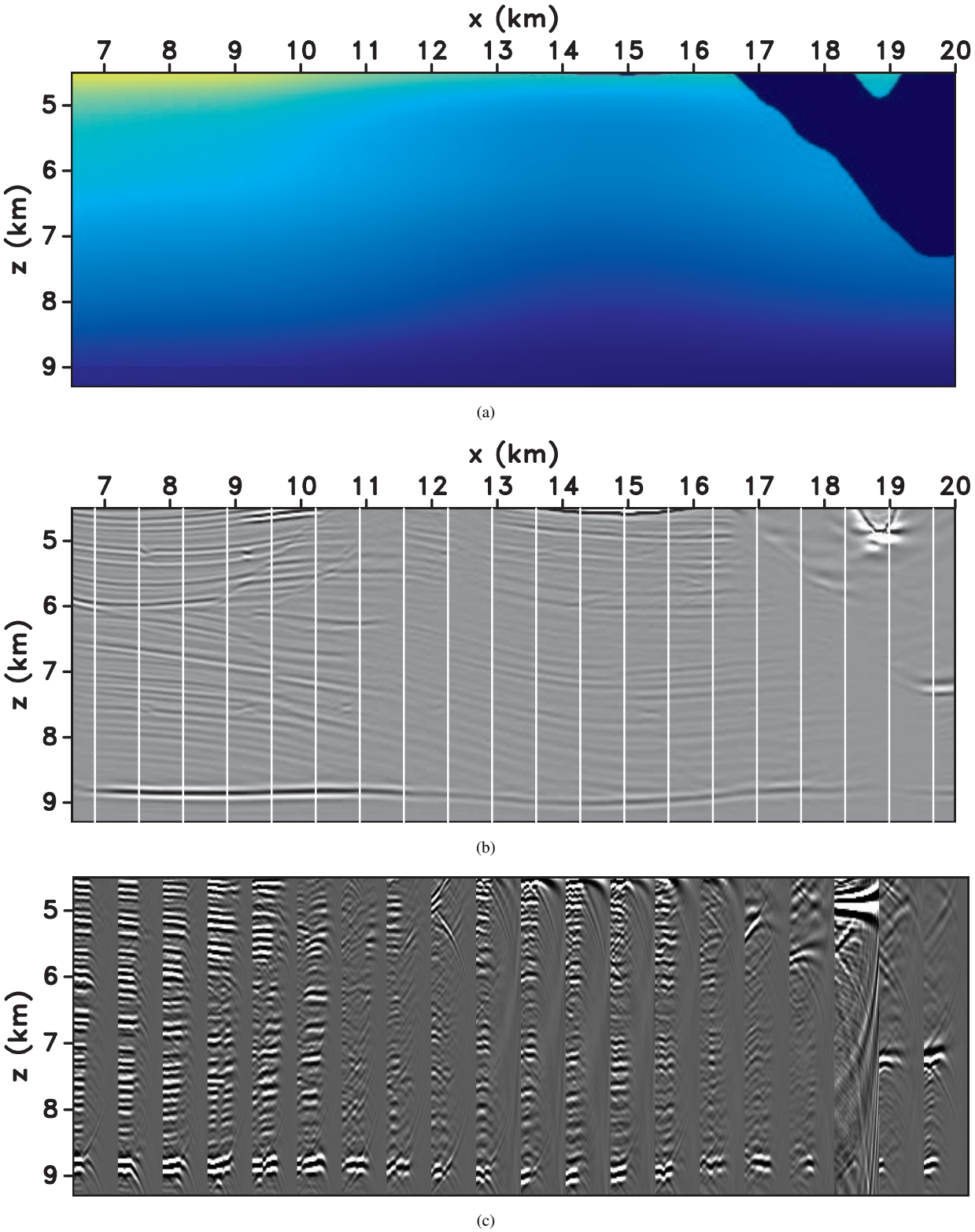


Figure 10. (a) The reconstructed model from inversion using the DSO penalty. (b) The migrated image, and (c) the angle-domain gathers obtained using the reconstructed model.

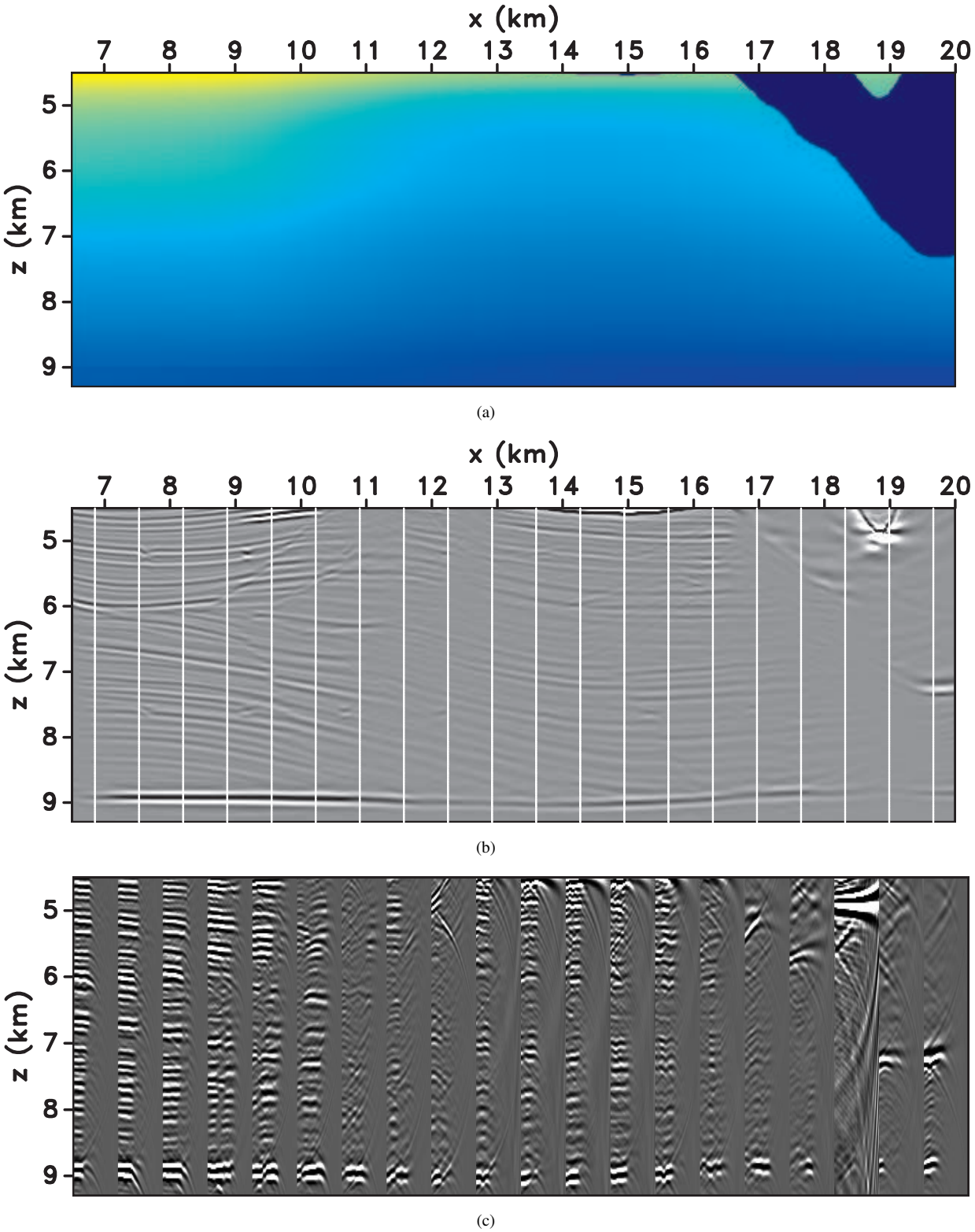


Figure 11. (a) The reconstructed model from inversion using the illumination-based penalty. (b) The migrated image, and (c) the angle-domain gathers obtained using the reconstructed model.

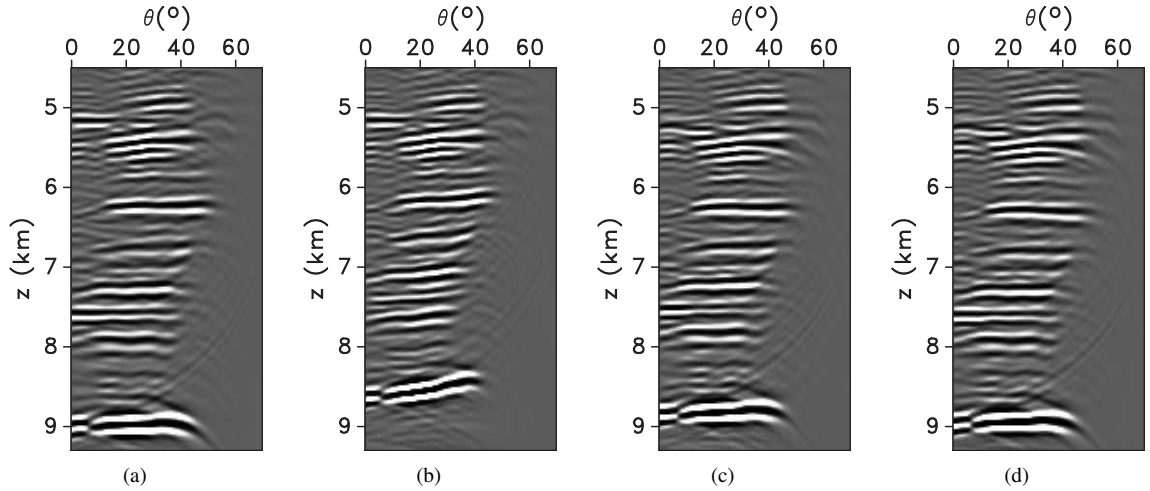


Figure 12. Angle-domain gathers at $x = 10.2$ km for (a) the correct model, (b) the initial model, (c) the reconstructed model using DSO penalty, and (d) the reconstructed model using the illumination-based penalty.

and illumination-based penalties. The gathers for both reconstructed models show flatter reflections, indicates that reconstructed models are more accurate than the initial model. We can, nonetheless, observe that the reflections in Figure 12(d) are flatter than those in Figure 12(c), and conclude that the reconstructed model using the illumination-based penalty is more accurate.

4 DISCUSSION

Uneven illumination is often a challenge faced by the exploration activities in complex subsurface environments, particularly in sub-salt areas. Furthermore, imperfect acquisition can also cause illumination problems. Essentially, the core of the illumination problem is that the reflections from various angles cannot be observed on the surface, either because of the complexity of the subsurface or because of limited/partial acquisition on the surface. In both situations, the effectiveness of image-domain wavefield tomography deteriorates as the imbalanced illumination creates defocusing in space-lag gathers regardless of the accuracy of the velocity model. Minimizing such defocusing through wavefield tomography generates incorrect updates and artifacts in the result. Therefore, the defocusing caused by the uneven illumination must be excluded from the model building process. This is done by replacing the DSO penalty operator with a modified penalty operator, which is constructed based on the illumination information. This penalty operator differentiates between the defocusing caused by uneven illumination and that due to model errors and therefore does not penalize the defocusing due to the illumination. During our iterative inversion, we update penalty operator at each iteration, as the velocity model is changing during the iterations and the subsurface illumination information needs to be re-evaluated.

In the theory section, we discuss the formulation of image-domain wavefield tomography and our solution to illumination problems based on a two-way wave equation. The formulation, however, applies well when a one-way wave equation is used. The construction of the illumination-based penalty operator is similar, except for the wave equation used in all modeling and migrations.

5 CONCLUSIONS

We demonstrate an illumination compensation strategy for wavefield tomography in the image domain. The idea is to measure the illumination effects on space-lag extended images, and replace the conventional DSO penalty operator with another one that compensates for illumination. This approach isolates the defocusing caused by the illumination such that image-domain wavefield tomography minimizes only the defocusing relevant to the velocity error. Synthetic examples demonstrate the negative effects of uneven illumination on the reconstructed model and show the improvements on both the inversion results and on the migrated images after the illumination information is included in the penalty operator. Our approach enhances the robustness and effectiveness of wavefield tomography in the model building process when the surface data are incomplete or when the subsurface illumination is uneven due to complex geologic structures such as salt.

6 ACKNOWLEDGMENTS

We acknowledge the support of the sponsors of the Center for Wave Phenomena at Colorado School of Mines. The reproducible numeric examples in this paper use the Madagascar open-source software package freely available from http://www.reproducibility.org. This research was supported in part by the Golden Energy Computing Organization at the Colorado School of Mines using resources acquired with financial

assistance from the National Science Foundation and the National Renewable Energy Laboratory.

REFERENCES

Al-Yahya, K., 1989, Velocity analysis by iterative profile migration: Geophysics, **54**, 718–729.

Biondi, B., and W. Symes, 2004, Angle-domain common-image gathers for migration velocity analysis by wavefield-continuation imaging: Geophysics, **69**, 1283–1298.

Etgen, J., S. H. Gray, and Y. Zhang, 2009, An overview of depth imaging in exploration geophysics: Geophysics, **74**, WCA5–WCA17.

Gherasim, M., U. Albertin, B. Nolte, and O. Askim, 2010, Wave-equation angle-based illumination weighting for optimized subsalt imaging: Presented at the 80th Annual International Meeting, SEG, Expanded Abstracts.

Gray, S. H., J. Etgen, J. Dellinger, and D. Whitmore, 2001, Seismic migration problems and solutions: Geophysics, **66**, 1622–1640.

Guitton, A., 2004, Amplitude and kinematic corrections of migrated images for nonunitary imaging operators: Geophysics, **69**, 1017–1024.

Knyazev, A. V., and I. Lashuk, 2007, Steepest descent and conjugate gradient methods with variable preconditioning: Matrix Analysis and Applications, **29**, 1267–1280.

Leveille, J. P., I. F. Jones, Z. Z. Zhou, B. Wang, and F. Liu, 2011, Subsalt imaging for exploration, production, and development: A review: Geophysics, **76**, WB3–WB20.

Nemeth, T., C. Wu, and G. T. Schuster, 1999, Least-square migration of incomplete reflection data: Geophysics, **64**, 208–221.

Paffenholz, J., B. McLain, J. Zaske, and P. Keliher, 2002, Subsalt multiple attenuation and imaging: Observations from the sigsbee 2b synthetic dataset: 72nd Annual International Meeting, SEG, Expanded Abstracts, 2122–2125.

Plessix, R.-E., 2006, A review of the adjoint state method for computing the gradient of a functional with geophysical applications: Geophysical Journal International, **167**, 495–503.

———, 2009, Three-dimensional frequency-domain full-waveform inversion with an iterative solver: Geophysics, **74**, WCC53–WCC61.

Pratt, R. G., 1999, Seismic waveform inversion in the frequency domain, Part 1: Theory and verification in a physical scale model: Geophysics, **64**, 888–901.

Rickett, J., and P. Sava, 2002, Offset and angle-domain common image-point gathers for shot-profile migration: Geophysics, **67**, 883–889.

Sava, P., and S. Fomel, 2003, Angle-domain common image gathers by wavefield continuation methods: Geophysics, **68**, 1065–1074.

Shen, H., S. Mothi, and U. Albertin, 2011, Improving subsalt imaging with illumination-based weighting of rtm 3d angle gathers: Presented at the 81th Annual International Meeting, SEG, Expanded Abstracts.

Shen, P., and H. Calandra, 2005, One-way waveform inversion within the framework of adjoint state differential migration: 75th Annual International Meeting, SEG, Expanded Abstracts, 1709–1712.

Shen, P., C. Stolk, and W. Symes, 2003, Automatic velocity analysis by differential semblance optimization: 73th Annual International Meeting, SEG, Expanded Abstracts, 2132–2135.

Shen, P., and W. W. Symes, 2008, Automatic velocity analysis via shot profile migration: Geophysics, **73**, VE49–VE59.

Sirgue, L., and R. Pratt, 2004, Efficient waveform inversion and imaging: A strategy for selecting temporal frequencies: Geophysics, **69**, 231–248.

Stolk, C. C., and W. W. Symes, 2004, Kinematic artifacts in prestack depth migration: Geophysics, **69**, 562–575.

Symes, W., 2009, Migration velocity analysis and waveform inversion: Geophysical Prospecting, **56**, 765–790.

Symes, W. W., 2008, Migration velocity analysis and waveform inversion: Geophysical Prospecting, **56**, 765–790.

Symes, W. W., and J. J. Carazzone, 1991, Velocity inversion by differential semblance optimization: Geophysics, **56**, 654–663.

Tang, Y., and B. Biondi, 2011, Target-oriented wavefield tomography using synthesized born data: Geophysics, **76**, WB191–WB207.

Tarantola, A., 1984, Inversion of seismic reflection data in the acoustic approximation: Geophysics, **49**, 1259–1266.

Vigh, D., and E. W. Starr, 2008, 3D prestack plane-wave, full-waveform inversion: Geophysics, **73**, VE135–VE144.

Virieux, J., and S. Operto, 2009, An overview of full-waveform inversion in exploration geophysics: Geophysics, **74**, WCC1–WCC26.

Woodward, M., D. Nichols, O. Zdraveva, P. Whitfield, and T. Johns, 2008, A decade of tomography: Geophysics, **73**, VE5–VE11.

Woodward, M. J., 1992, Wave-equation tomography: Geophysics, **57**, 15–26.

Yang, T., and P. Sava, 2010, Moveout analysis of wave-equation extended images: Geophysics, **75**, 151–161.

Yilmaz, O., 2001, Seismic Data Analysis (2nd edition): Society of Exploration Geophysicists.

Yu, J., and T. Schuster, 2003, Migration deconvolution vs. least squares migration: Presented at the 74th Annual International Meeting, SEG, Expanded Abstracts.